Magnetic exchange and dipolar interactions in $GdRu_2Si_2$: Three-dimensional magnetism in a layered magnet

Sagar Sarkar [1,*] Rohit Pathak [1] Arnob Mukherjee [1] Anna Delin [2,3,4] Olle Eriksson,[1,5] and Vladislav Borisov [1,5,†]

[1]*Department of Physics and Astronomy, Uppsala University, 751 20 Uppsala, Sweden*

[2]*Department of Applied Physics, School of Engineering Sciences, KTH Royal Institute of Technology, AlbaNova University Center, SE-10691 Stockholm, Sweden*

[3]*Wallenberg Initiative Materials Science for Sustainability (WISE), KTH Royal Institute of Technology, SE-10044 Stockholm, Sweden*

[4]*SeRC (Swedish e-Science Research Center), KTH Royal Institute of Technology, SE-10044 Stockholm, Sweden*

[5]*Wallenberg Initiative Materials Science for Sustainability, Uppsala University, 75121 Uppsala, Sweden*

(Received 3 June 2025; revised 20 August 2025; accepted 19 September 2025; published 7 October 2025)

$GdRu_2Si_2$ has recently drawn significant attention as a centrosymmetric magnet capable of hosting a short-period skyrmion square lattice (SkL) in the absence of Dzyaloshinskii-Moriya interaction (DMI). In this system, Gd atoms are arranged on a square lattice, forming 2D layers separated by the Ru-Si network in the out-of-plane direction. RKKY-type exchange between the Gd moments results in an exchange frustration, which is the main source of non-collinearity in the spiral phases of the system. So far, the literature has emphasized the importance of in-plane $\vec{Q}$ vectors in understanding the magnetic phases of the system as they appear and have been observed in the 2D Gd layers. In this work, we calculate the Gd-Gd magnetic exchange interactions (J_{ij}) and perform atomic spin dynamics (ASD) simulations, providing new insights about $GdRu_2Si_2$. Our calculated J_{ij} shows that the strongest magnetic interaction occurs between Gd atoms along the [111] body-diagonal direction of the unit cell. This, along with the body-centered tetragonal structure of the Gd sublattice, points to the presence of a hitherto ignored modulation vector, $\vec{Q}_{[111]}$, along the [111] direction in the spiral phases of the system. We confirm this with ASD simulations and establish that the magnetic phases in $GdRu_2Si_2$ are far more complex than they appear to be in the 2D Gd layers. This interlayer modulation vector $\vec{Q}_{[111]}$, along with the intralayer $\vec{Q}_{[100]}$ and $\vec{Q}_{[010]}$, determines the total magnetic ordering of the system. Despite its layered appearance, both structurally and magnetically, it is in reality a strong 3D magnet, requiring additional considerations for its proper theoretical modeling. Taking these into account, our ASD simulations provide an excellent description of the experimentally observed magnetic phase transitions. Furthermore, our work reveals the critical influence of dipolar interactions on the ground-state magnetic properties of $GdRu_2Si_2$, a direct consequence of the large magnetic moment of Gd. We observed a competition between dipolar interactions and uniaxial anisotropy, with each favoring a different magnetic ordering. However, the dominance of the dipolar interaction is evident in the observed ground state. This suggests a weak uniaxial anisotropy in the system, which aligns with the spherical symmetry of the Gd $4f$ states. Our findings offer a deeper understanding of $GdRu_2Si_2$'s complex magnetism and highlight the potential for similar important interlayer effects in other layered magnetic systems.

DOI: 10.1103/q853-plvr

I. INTRODUCTION

$GdRu_2Si_2$ is a magnetic metallic system that has recently attracted attention, along with some analogous systems, due to its interesting magnetic properties. The main source of magnetism here is the localized half-filled Gd $4f$ orbitals resulting in a large spin moment of $7\,\mu_B$ [1]. The delocalized Gd $5d$ and Ru $4d$ states, on the other hand, create a pool of conduction electrons leading to metallicity and magnetic exchange interactions between the Gd $4f$ moments via the RKKY mechanism [2]. Although Gd is a relatively heavy element, with expected large spin-orbit effects, the presence of inversion symmetry forbids the emergence of Dzyaloshinskii-Moriya interaction (DMI) [3,4], which is a widely discussed chiral interaction. As a result, the Heisenberg exchange becomes the dominant mechanism of spin-spin interactions which may potentially provide noncollinear textures in $GdRu_2Si_2$, as we will investigate in detail in this work.

Like any magnetic system, the magnetic properties of $GdRu_2Si_2$ depend on temperature (T) and external magnetic field (B). This particular system, however, shows an interesting and rich B-T phase diagram consisting of different phases

*Contact author: sagar.sarkar@physics.uu.se

†Contact author: vladislav.borisov@physics.uu.se

Published by the American Physical Society under the terms of the Creative Commons Attribution 4.0 International license. Further distribution of this work must maintain attribution to the author(s) and the published article's title, journal citation, and DOI. Funded by Bibsam.

[5]. The primary interest is the square skyrmion lattice (SkL) phase that appears in the low-T regime within a narrow range of external magnetic fields around 2T.

Magnetic skyrmions are topological solitons with a topological charge defined by the so-called skyrmion number N_{sk} [6]. The spin ordering in a skyrmion can be considered as a special arrangement of 3D spins on a 2D plane in such a manner that they could be mapped back on the surface of a sphere [6,7]. A periodic arrangement of these skyrmions is referred to as a skyrmion crystal (SkX) that shows unconventional magnetic and transport properties [7–11]. This makes them promising candidates for future memory devices and spintronics applications [12]. SkX is not something new and has previously been observed in chiral magnets [13] such as MnSi, FeGe, and Cu_2OSeO_3 [14–19]. In these chiral magnets, the noncollinearity of the spins in the SkX results from a competition between exchange and DMI, leading to skyrmions with a large size between 20 and 100 nm [15,20].

What makes $GdRu_2Si_2$ special compared to these known skyrmionic systems is that SkL results mainly from exchange frustration without DMI [13,21]. This results in much smaller skyrmions of around 2 nm in the SkL phase [5,21]. The smaller size of these topological objects theoretically means a higher surface density and better device applicability, although single skyrmions not arranged in a lattice, which would be necessary for applications, have not yet been observed in $GdRu_2Si_2$. Hence, the ongoing efforts aim to understand, from a fundamental point of view, the magnetic properties of this system. This would aid in tuning the position of the SkL phase in the B-T phase diagram. This is part of an emerging field of scientific research intending to understand the microscopic electronic and magnetic properties behind the stabilization of the SkL phase in systems without DMI. As discussed in the literature, the microscopic origin of the noncollinearity in the spiral phases is the exchange frustration due to the RKKY mechanism [2]. To obtain a quantitative understanding of the exchange frustration, Nomoto *et al.* [13] performed an orbital decomposition of the calculated Gd-Gd exchange J_{ij}. The Fourier transform $J(q)$ of the orbital-decomposed exchange revealed an FM and AFM ground state for the $5d$-$5d$ and $4f$-$4f$ components, respectively. The presence of these competing interactions was claimed to be the reason for noncollinearity due to exchange frustration. However, in order to correctly describe the exact nature or spin configuration of the spiral states, other interactions along with exchange frustration were necessary. For example, the recent theoretical study by Boujziz *et al.* [21] reported the importance of uniaxial magnetocrystalline anisotropy (K_U) for the stability of the SkL phase in this system. Rapid progress in the $GdRu_2Si_2$ study made new revelations and provided new insights about the magnetic phases. Initially, the zero-field ground state of the system was reported to be a helical spiral with a single-**Q** modulation [5]. However, recent experimental studies with more advanced techniques confirmed a double-**Q** modulated ground state [22–24]. For such a state, additional interactions beyond exchange frustration and uniaxial anisotropy were suggested. The importance of four-spin (biquadratic) interaction mediated by itinerant electrons in the presence of easy axis anisotropy has been claimed from the very beginning [5,22,25] for a double-**Q** phase that could transform to a topological SkL phase under a magnetic field. It should be noted that four-spin interactions are often discussed for itinerant magnets since they are the lowest-order interactions beyond the Heisenberg exchange that can be significant enough to affect the magnetic order. Though a consensus has not yet been achieved as to what drives the skyrmion formation, there is a general agreement regarding the characterization of different magnetic phases in terms of the modulation vectors. The two in-plane modulation vectors $\mathbf{Q}_{100}$ along **a** axis and $\mathbf{Q}_{010}$ along **b** axis have been considered important and are enough to describe the magnetic phases. This is because each phase appears and has been observed in the two-dimensional (2D) layers of the Gd square lattice.

In this report, we calculate and analyze in detail the magnetic exchange interactions in this layered rare-earth system $GdRu_2Si_2$. We show that the magnetic phases are more complex than what was discussed in the literature so far and cannot be described with the in-plane modulation vectors alone. The calculated exchange interactions indicate, for example, that the exchange frustration results from competition between the intralayer and interlayer exchange, where the latter was mostly neglected in previous studies. A stronger interlayer FM exchange along with the body-centered tetragonal Gd sublattice results in an interlayer modulation vector $\mathbf{Q}_{111}$ along the [111] body-diagonal direction of the unit cell which we confirm using atomistic spin dynamics (ASD) simulations. The $\mathbf{Q}_{111}$ modulation of the spin texture cannot be neglected while simulating the magnetic phase diagram, since ASD simulation for a supercell incompatible with $\mathbf{Q}_{111}$ does not show the experimentally observed magnetic phase transitions as a function of applied magnetic field **B**. From these simulations, we confirm the importance of dipolar interactions that govern the ground-state magnetic properties of the system. A competing effect of the dipolar interaction and uniaxial anisotropy was found, where both try to stabilize different magnetic orderings. The dominance of the dipolar interaction over uniaxial anisotropy becomes evident from the ground-state properties. This indirectly points to a weak uniaxial anisotropy consistent with the spherical symmetry of the Gd $4f$ states. However, stabilization of the critical SkL phase might still require other weak interactions like biquadratic and symmetric anisotropic exchange acting as a perturbation.

While our work is about a concrete magnetic system, the discussion of magnetic phases and theoretical approaches for their simulation is quite general and can be applied to many other noncollinear magnets with spiral or skyrmion phases. In particular, using $GdRu_2Si_2$ as an example, we point out some important aspects of our methodology that are required to correctly model the magnetic phase diagram using atomistic spin dynamics (ASD). Since ASD is widely used nowadays for studying magnets, the methodological conclusions of our study can make a useful contribution to the field in general. It is also worthwhile to mention that $GdRu_2Si_2$ has a very common type of crystal structure, the so-called 122- or $ThCr_2Si_2$-type of structure, which is also found in widely discussed iron-based superconductors and magnets [26] and rare-earth magnets $LnRh_2Si_2$ with ultrafast demagnetization dynamics [27] (see further examples in Ref. [28]).

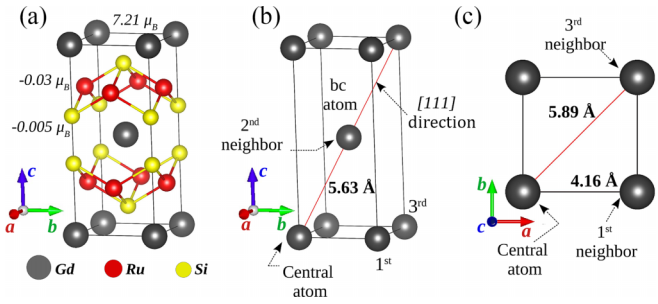


FIG. 1. (a) The experimental tetragonal unit cell of $GdRu_2Si_2$ with almost a layered structure. The 2D Gd layers are separated from each other by the Ru-Si networks along the c axis. The magnetic moments of each atom are also indicated, which were obtained from DFT calculations described in Sec. III B. (b) Position of the Gd atoms in the unit cell showing the formation of a body-centered tetragonal sublattice. The second neighbor direction and the corresponding Gd-Gd distance are shown. (c) Square lattice arrangement of the Gd atoms in the ab plane of a single Gd layer. The in-plane nearest neighbor and third neighbor directions and corresponding Gd-Gd distances are shown.

The paper is organized as follows. Section II details our computational methodology. In Sec. III, we present and discuss the results on the structural, electronic, and magnetic properties of $GdRu_2Si_2$. Finally, Sec. IV provides the concluding remarks.

II. METHODOLOGY

A. Electronic structure and magnetic exchange

We have considered the two-formula unit tetragonal unit cell for our system. The lattice parameters were kept fixed at the experimental values [29]. First, we have calculated the electronic structure from density functional theory (DFT) using a projected augmented wave (PAW) method [30,31] as implemented in the Vienna *ab initio* simulation package (VASP) [32–35]. The generalized gradient approximation (GGA) [36] in the Perdew-Burke-Ernzerhof (PBE) parametrization [36,37] was considered for the exchange-correlation functional and a plane-wave energy cutoff of 500 eV was used for the basis set. Along with this, a Γ-centered Monkhorst-Pack $20 \times 20 \times 10$ **k** mesh, providing convergence of the total energy and local moments, was used for reciprocal space integration. The main purpose was to check the effect of the crystalline environment and other delocalized s, p, and d states on the atomic-like localized Gd $4f$ states. For this, the Gd $4f$ states were considered as part of the valence electronic manifold, and to achieve a correct description of their localized nature, we have performed a DFT+U calculation within the Hartree-Fock approximation [38,39]. For this, the rotationally invariant formulation of Liechtenstein *et al.* [40] was used with the Coulomb interaction parameters $U = 6.7$ eV and $J = 0.7$ eV on the Gd $4f$ states, based on a previous study [41]. Calculations based on this methodology were used here for an initial analysis of electronic properties presented also in Fig. 2.

Following this, to extract the magnetic exchange interactions between the Gd moments, the electronic structure was

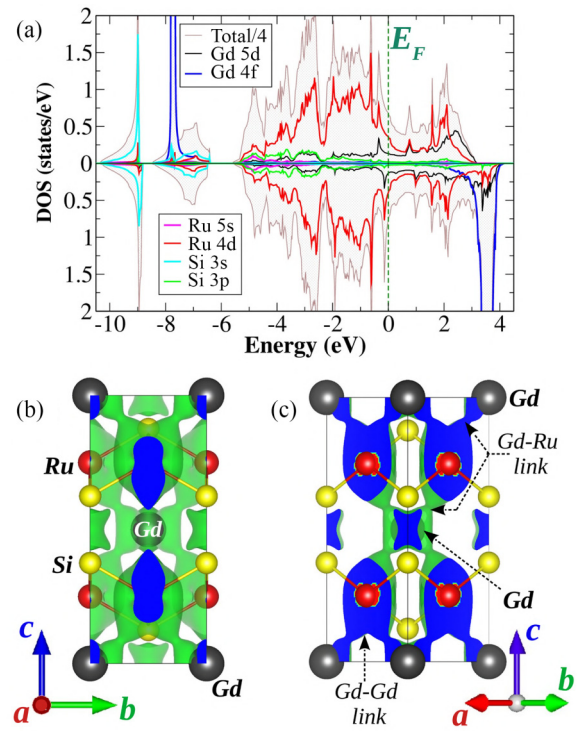


FIG. 2. (a) Total (scaled down by 4) and atom+orbital projected density of states from VASP calculation where Gd $4f$ states were treated as valence states. See the main text for details. (b) and (c) show the charge density distribution corresponding to the valence states around Fermi energy along [100] and [110] directions, respectively. See the main text for more details.

again calculated with the full potential linear muffin-tin orbital (FP-LMTO) method, as implemented in the RSPT software [42–45]. GGA-PBE exchange-correlation functional was used similarly to the VASP calculations. These calculations included two sets of basis functions, covering both valence and semicore states. These states were specifically constructed from the $6s$, $6p$, and $5d$ orbitals for Gd and Ru, and the $3s$, $3p$, and $3d$ orbitals for Se, respectively. The Gd $4f$ states were considered in the core to be treated scalar relativistically to reduce the computational cost. Hence, a DFT+U calculation was not required in this case. The Gd $4f$ states, with their large binding energy and strong spin polarization, result in a significant magnetic moment of $7\mu_B$. In our VASP calculations, we incorporate these properties using the DFT+U method and confirm the noninteracting localized nature of the Gd $4f$ states (see Sec. I of Supplemental Material (SM) Ref. [46]). For RSPT calculations, while DFT+U is a viable option, a frozen-core approximation that treats the fully spin-polarized $4f$ states as core electrons is also highly effective [47]. This approach is particularly accurate for Gd because of its negligible orbital moment, making it well-suited for studying the ground-state electronic structure and magnetic interactions. However, it is important to note that this approximation would be invalid for studying excitation spectra. We chose the kinetic tail energies of −0.1, −2.3, and 1.5 Ry. For the Brillouin zone sampling, we used an optimized Γ-centered Monkhorst-Pack mesh of $32 \times 32 \times 16$ **k** points. From here, the *ab initio* Kohn-Sham Hamiltonian or the DFT Hamiltonian is mapped onto an

effective Heisenberg Hamiltonian with classical spins of the following form [48,49] to extract the interatomic exchange interactions through the application of the magnetic force theorem (MFT) [48,50] (for a review, see Ref. [51]):

$$H = -\sum_{i \neq j} J_{ij}\, \vec{e}_i \cdot \vec{e}_j. \tag{1}$$

Here, (i, j) are the indices for the magnetic sites in the system, while $\vec{e}_i$ and $\vec{e}_j$ are the unit vectors along the spin directions at the sites i, and j, respectively; J_{ij} is the exchange interaction between the two spins at the sites i and j. In the Green-function-based approach to evaluate the J_{ij} values used in the RSPT software, the exchange parameters J_{ij} are determined from a generalized nonrelativistic expression as given below [49].

$$J_{ij} = \frac{T}{4} \sum_{n} \mathrm{Tr}[\hat{\Delta}_i(i\omega_n)\hat{G}^{\uparrow}_{ij}(i\omega_n)\hat{\Delta}_j(i\omega_n)\hat{G}^{\downarrow}_{ji}(i\omega_n)]. \tag{2}$$

Here T is the temperature, and $\hat{\Delta}$ is the onsite exchange potential giving the exchange splitting at sites i and j; $\hat{G}^{\sigma}_{ij}$ is the intersite Green's function projected over spin σ that can have values $\{\uparrow, \downarrow\}$ and ω_n is the nth fermionic Matsubara frequency. All the terms in the above expression are matrices in orbital and spin space with the trace running over the orbital degrees of freedom. The summation is over Matsubara frequencies (ω_n). To ensure precise convergence in our analysis of exchange parameters, we increased the k-mesh to $52 \times 52 \times 26$ for these calculations. We note that the exchange interactions in this system are very similar within the nonrelativistic and fully-relativistic limits (see a comparison in Sec. II of SM Ref. [46]).

We employed the force theorem to determine the magnetic anisotropy, as this method has greater efficiency and accuracy from a computational point of view compared to the method based on total magnetic energies for different orientations of the global spin axis, as discussed, e.g., in previous works [52,53].

In this approach, we first conducted nonrelativistic self-consistent DFT calculations using the RSPT code. Once we obtained the converged potential and charge density, we performed three fully relativistic non-self-consistent (single-iteration) calculations with magnetic moments aligned along the three mutually orthogonal [100], [010], and [001] Cartesian directions. The magnetic anisotropy energy (MAE) was then calculated by taking the difference between the eigenvalue sums for the in-plane and out-of-plane magnetic moment directions. For the MAE calculations, we used a converged $60 \times 60 \times 30$ k mesh, slightly finer than for the J_{ij} calculation.

B. Atomistic spin dynamics simulations

In the next step, spin textures were simulated by atomistic spin dynamics (ASD) using the Uppsala atomistic spin dynamics (UPPASD) package [54,55], where also the inclusion of spin-lattice coupling effects can be done in a systematic first-principles way following the methodology in [56].

In this work, we focus on the spin part of the system and solve the Landau-Lifshitz-Gilbert (LLG) equation [57,58] for the atomic magnetic moments:

$$\frac{d\vec{m}_i}{dt} = -\frac{\gamma}{1+\alpha^2}\,\vec{m}_i \times [\vec{B}_i + \vec{b}_i(t)] - \frac{\gamma}{m_i}\frac{\alpha}{1+\alpha^2}\,\vec{m}_i \times (\vec{m}_i \times [\vec{B}_i + \vec{b}_i(t)]). \tag{3}$$

Here, γ is the gyromagnetic ratio, and $\vec{b}_i(t)$ is a stochastic magnetic field with Gaussian distribution. The magnitude of this field is related to the damping parameter α, which helps bring the system into thermal equilibrium, and temperature T. We use a time step of $\Delta t = 0.1$fs for the annealing phase and $\Delta t = 1$fs for the measurement phase in the UPPASD calculations to solve these differential equations.

The effective field $\vec{B}_i$ experienced by each spin i is derived from the partial derivative of the Hamiltonian H with respect to the local magnetic moment,

$$\vec{B}_i = -\frac{\partial H}{\partial \vec{m}_i}. \tag{4}$$

The Hamiltonian H includes all relevant interactions and is given by

$$H = -\frac{1}{2}\sum_{i \neq j} J_{ij}\, \vec{e}_i \cdot \vec{e}_j - K_U \sum_i (\vec{e}_i \cdot \vec{z}\,)^2 - \sum_i \vec{B}_{\mathrm{ext}} \cdot \vec{e}_i, \tag{5}$$

where the first term describes the Heisenberg exchange, the second term is the uniaxial anisotropy, and the final term corresponds to the effect of an external field $\vec{B}_{\mathrm{ext}}$. For small $\vec{B}_{\mathrm{ext}}$, the most significant contribution to the Hamiltonian is typically from Heisenberg exchange interaction, where i and j are atomic indices, and J_{ij} is the strength of the exchange interaction, obtained from our first-principles calculations. For a magnetic system like $GdRu_2Si_2$ with large atomic spins of $7\mu_B$, dipolar interactions could become important. For this, the following interaction term H_{dip} was added to our Hamiltonian in Eq. (5) as required.

$$H_{\mathrm{dip}} = -\frac{\mu_0}{4\pi}\sum_{i \neq j} \frac{1}{r_{ij}^3}[3(\mathbf{m}_i \cdot \hat{r}_{ij})(\mathbf{m}_j \cdot \hat{r}_{ij}) - \mathbf{m}_i \cdot \mathbf{m}_j], \tag{6}$$

where $\mathbf{m}_i$ and $\mathbf{m}_j$ are the atomic moments at sites i and j, respectively, and μ_0 is the magnetic constant. For the calculation of this term, we used an FFT-based implementation, available in the UPPASD code, based on the approach described by Hayashi *et al.* in Ref. [59].

While Eqs. (3), (4), and (6) contain the atomic moments $\vec{m}_i$, the spin model (5) is defined in terms of unit vectors $\vec{e}_i$, and the relation between these two quantities is $\vec{m}_i = |m_i|\vec{e}_i$, where $|m_i|$ is the magnitude of the atomic moment for a particular site. For that reason, the moment magnitude is absorbed in the definition of magnetic exchange interactions J_{ij}, on-site anisotropy K_U and external field $\vec{B}_{\mathrm{ext}}$ in Eq. (5).

In the atomistic spin dynamics (ASD) simulation, we used a periodic simulation box with a size of, for example, $37 \times 37 \times 37$ conventional unit cells with 2 Gd atoms per cell, resulting in 101 306 spins. We first performed a simulated annealing to bring the system into thermal equilibrium, followed by an ASD measurement phase to obtain the spin texture after the system had evolved via the LLG equation and reached an energy minimum. Simulated annealing was performed at

gradually decreasing temperatures of 200, 100, 50, and 10K, with 20 000 spin-dynamics sampling steps at each temperature. After these annealing steps, we performed 500 000 sampling steps during the measurement phase, so that the spin system can reach an equilibrium state at zero temperature and a given external magnetic field.

III. RESULTS AND DISCUSSION

This section is divided into three sections: A–C, which discuss the structural, electronic, and magnetic properties of $GdRu_2Si_2$, respectively.

A. Structural properties

We start with the structural details of $GdRu_2Si_2$, and the experimental unit cell [29] that is shown in Fig. 1(a). In this system, the Gd atoms are the main source of magnetism. The Gd sublattice forms a body-centered tetragonal structure (bct), as shown in Fig. 1(b). Hence, we can see that the structure becomes quite interesting with layers of Gd atoms stacked along the **c**-axis and separated from each other by the metallic Ru-Si networks. This initially gives an impression of a layered quasi-two-dimensional magnetic structure. However, that is far from reality, as we show in the present work. This will be evident when we discuss the magnetic properties of the system. Each Gd layer separated by the Ru-Si network discussed above forms a 2D square lattice, as shown in Fig. 1(c). The tetragonality ratio c/a of the system is such that the Gd atom in the body-centered position along the [111] direction of the unit cell becomes the second neighbor atom for the central atom, as indicated in Fig. 1(b). The third neighbor atom lies along the [110] in-plane direction of the square lattice, as pointed out in Fig. 1(c). The first, second, and third neighbors are shown here in the structural description as they become important in understanding the magnetic exchange and the magnetic properties.

B. Electronic properties

Next, we briefly discuss the basic electronic properties of the system. For this, we consider the unit cell shown in Fig. 1(a) with FM ordering of the Gd spins. nonrelativistic GGA+U calculation was performed in VASP considering the Gd $4f$ states in the valence with the values of U and J equal to 6.70 and 0.70 eV, respectively [41]. The aim was to check the interaction between the $4f$ and other valence states of the system. The calculated total density of states (DOS) and atom-projected partial density of states (PDOS) are shown in Fig. 2(a). From these plots, we can see that the system is metallic. Although we have an FM order, the exchange splitting of the states near the Fermi energy (E_F) is weak. This results in tiny induced moments on the Ru and Si atoms, as indicated in Fig. 1(a). Large exchange splitting due to FM order is visible only for the localized Gd $4f$ states (blue lines) far away from E_F and resulting in a large spin of $7\mu_B$. Major contributions at E_F come from the Ru $4d$ (about 65%) and Gd $5d$ (about 30%) states, as shown by the red and black lines, respectively. Si $3p$ states (green line) have a minimal contribution around E_F and can be ignored. These states form a pool of conduction electrons distributed within the system. To verify the nature of this distribution, a small energy window of 0.20 eV was considered around the Fermi level, and the charge density (CD) corresponding to these states was calculated as shown in Figs. 2(b) and 2(c) from two different angles. An isosurface level was selected in such a way as to make the CD visible around both the Ru and Gd atoms. The charge density does not show a layered-type structure localized in the individual Gd and Ru-Si atomic layers. We can see prominent links connecting the charge densities around the Gd and Ru atoms, as shown in Fig. 2(c). Most importantly, a strong intralayer contact between the Gd atoms via the CD is missing. Instead, the Gd atoms get connected indirectly via the Ru atoms. On the other hand, the conduction electrons are the main source in this system for mediating magnetic exchange between Gd atoms, and these interactions have been suggested to have an RKKY character [2]. For that reason, the anisotropic structure of the conduction electron density is expected to impact the magnetic exchange interactions which we discuss in the next section.

C. Magnetic properties

This subsection is dedicated to presenting and discussing our calculated magnetic data and the core results of our work. For enhanced clarity, this discussion is structured into three segments. The initial segment focuses on establishing the 3D magnetism of $GdRu_2Si_2$ based on exchange analysis. The second segment utilizes ASD simulations to corroborate the 3D nature of any spiral phases arising from exchange frustration. The third segment conducts a systematic investigation to elucidate the importance of dipolar interactions in determining the magnetic ground state of $GdRu_2Si_2$.

1. Magnetic exchange and 3D magnetism of $GdRu_2Si_2$

Calculation of magnetic exchange interactions. In the next step, we calculated the magnetic exchange interactions for the FM reference state via magnetic force theorem (MFT) [48,50] (review in Ref. [51]) available in the RSPT software [42–44]. The Gd $4f$ states were treated as spin-polarized core states in this calculation since they represent nonhybridized, localized electron states, a configuration of the $4f$ states that closely represents the so-called Standard model of the rare-earths [60]. Note that a more precise treatment would involve the so-called Hubbard-I approximation, which was investigated for the rare-earth elements in detail in Ref. [47]. However, for Gd-based systems, where the spin-up $4f$ shell is filled and spherically symmetric, treating the $4f$ states as a spin-polarized core or a spin-polarized valence band closely resembles the Hubbard-I approximation, which motivates the approximations used here. A comparison between VASP and RSPT calculated valence electronic states around the Fermi energy E_F is shown in Fig. S1 from Sec. I of SM Ref. [46].

RKKY-like exchange and key interactions. Magnetic interactions (J_{ij}) between Gd moments at different distances (d) (scaled by the lattice constant a) are shown in Fig. 3(a). We see a nearly alternating FM and AFM coupling with the neighboring atoms reminiscent of a free carrier-mediated RKKY type exchange [2], a well-known mechanism in intrinsic [61] and extrinsic [62,63] metallic magnets. RKKY has also been claimed in recent studies as the primary mechanism for

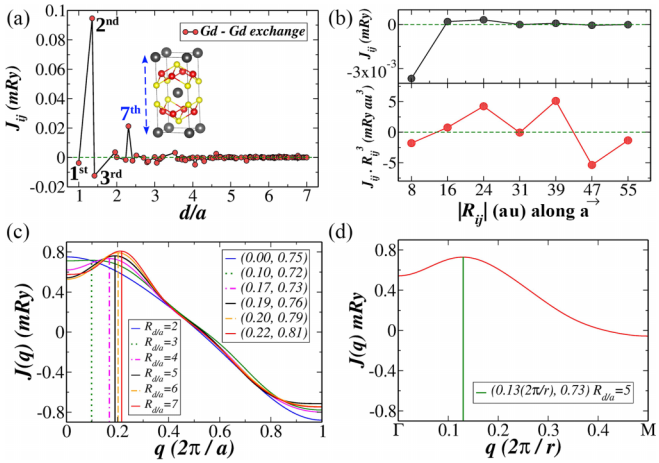


FIG. 3. (a) Calculated Gd-Gd interatomic exchange interactions as functions of distance d scaled by the lattice constant a. The inset depicts the exchange path corresponding to the seventh interaction in the out-of-plane direction. (b) As functions of distance R_{ij} along the crystallographic a axis, J_{ij} and $J_{ij} \cdot R_{ij}^3$ reveal oscillations which point at the RKKY exchange mechanism. (c) Fourier transforms $J(q)$ of the calculated exchange J_{ij} for $\mathbf{q}$ along $\mathbf{a}$ in the unit of $2\pi/a$ for different values of the cutoff radii $R_{d/a}$. The inset shows the $(|\mathbf{Q}_{100}|, J(|\mathbf{Q}_{100}|))$ values corresponding to the maxima of $J(q)$ (see the main text for details). (d) Fourier transform $J(q)$ of the calculated exchange J_{ij} for $\mathbf{q}$ along Γ-M direction of the Brillouin zone with $R_{d/a} = 5$. Γ-M direction is || to the [110] crystallographic direction.

magnetic interactions in this system [13,21,64]. To confirm this, we have separately plotted J_{ij} as a function of the interatomic distance R_{ij} along the in-plane $\mathbf{a}$ axis, as shown in the first panel of Fig. 3(b). Note that $J_{ij}(R_{ij})$ decays quickly, making it impossible to view its oscillatory properties. To overcome this and take into account the estimated scaling factor of $1/R_{ij}^3$ for RKKY interaction in metallic 3D systems [65], we plot $J_{ij} \cdot R_{ij}^3$ as a function of R_{ij} as shown in the bottom panel of Fig. 3(b). The resulting quantity $J_{ij} \cdot R_{ij}^3$ shows prominent oscillatory behavior revealing the RKKY-type exchange mechanism present in the system. Hence, long-ranged interatomic exchange with non-negligible interaction strength is not unexpected in this system as can be seen from Fig. 3(a), where the second (J_2) and seventh (J_7) interactions come out to be stronger than the first (J_1) and third (J_3) interactions. These four interactions are important and are discussed below in more detail. The first, second, and third neighbor exchange paths are shown in Fig. 1 and have been discussed in the previous sections. The seventh neighbor exchange path is shown in the inset of Fig. 3(a), which is along the $\mathbf{c}$-axis in the out-of-plane directions. To summarize, J_1 and J_3 are two intralayer exchange interactions that are weakly AFM, while J_2 and J_7, on the other hand, are two interlayer interactions that are FM in nature and stronger than the intralayer interactions. A stronger interlayer exchange suggests that the system should not be treated as a layered 2D magnetic system. Interlayer exchange, if considered alone, will stabilize an FM ordering without any magnetic frustration. However, the two intralayer AFM exchange interactions on the square lattice by symmetry may lead to an exchange frustration, and an overall noncollinear state could be found. This is in line with the experimental observation of noncollinear spiral states within the 2D Gd layers [5,22–24]. These states could be well described [22,66] by the two in-plane (IP) spin spiral modulation vectors $\mathbf{Q}_{100}$ and $\mathbf{Q}_{010}$ with the experimentally reported value $\mathbf{Q}_{100}^{\text{Exp}} = (0.22, 0, 0)$ along the $\mathbf{a}$ axis in the unit of reciprocal lattice vector $\mathbf{a}^*$ [5].

Stability of spin-spiral states. As the zero field spiral GS should mainly result from the Heisenberg exchange frustration in the absence of any DMI, a Fourier transform $J(q)$ of our calculated J_{ij}'s or the adiabatic magnon spectra (AMS) can predict such a modulation vector. This analysis, in turn, may confirm or refute the correctness of our calculated exchange interactions. In the $J(q)$ calculation, $R_{d/a}$ is a parameter defining the cut-off radii of a sphere around any magnetic site, measured in the unit of the lattice constant a. Only J_{ij}'s between that magnetic site and its neighbors inside the sphere are considered for the calculation of $J(q)$, and hence, it is expected to change with $R_{d/a}$. In Fig. 3(c), we show $J(q)$ for $\mathbf{q} \parallel \mathbf{a}$ in the units of reciprocal lattice vector $\mathbf{a}^*$, for different $R_{d/a}$ values. One can see that an FM stability only occurs for $R_{d/a} = 2$ and becomes unstable for $R_{d/a} \geqslant 3$ where a spin-spiral state with a modulation vector $\mathbf{Q}_{100}$ becomes favorable. $|\mathbf{Q}_{100}|$ is identified by the value of q where $J(q)$ reaches a maximum. For each considered $R_{d/a}$, the values $(|\mathbf{Q}_{100}|, J(|\mathbf{Q}_{100}|))$ are shown in the inset of Fig. 3(c). $\mathbf{Q}_{100}$ increases in magnitude gradually and becomes equal to the experimentally reported $\mathbf{Q}_{100}^{\text{Exp}}$ for $R_{d/a} = 7$. But since we can see from Fig. 3(a) that most of the calculated J_{ij}'s for $d/a \geqslant 5$ are nearly equal to zero, we have considered $R_{d/a} = 5$ for which $J(q)$ also predicts a spin-spiral modulation vector (0.19, 0, 0) very close to $\mathbf{Q}_{100}^{\text{Exp}}$. For a better understanding of the possible exchange spirals, we have also examined $J(q)$ for $\mathbf{q} \parallel$ different high-symmetry (HS) directions of the Brillouin zone (see Fig. S3 of SM Ref. [46] to view the Brillouin zone) and is presented in Fig. S4 of SM Ref. [46]. We found that $J(q)$ for $\mathbf{q}$ along Γ-$Y \parallel \mathbf{b}$ is identical to $\mathbf{q} \parallel \mathbf{a}$ showing $|\mathbf{Q}_{010}| = |\mathbf{Q}_{100}|$ with the same stabilization energy of 0.76 mRy/spin. This happens due to the in-plane square lattice symmetry of the Gd layers. These two vectors $\mathbf{Q}_{100}$ and $\mathbf{Q}_{010}$ also show the maximum stability over all other vectors. A close competition only comes from $\mathbf{Q}_{110}$ along Γ-$M \parallel$ to the in-plane crystallographic direction [110], for which the stabilization energy is 0.73 mRy/spin shown in Fig. 3(d). In summary, this suggests that the resulting zero-field exchange spiral should be governed by $\mathbf{Q}_{100}$ or $\mathbf{Q}_{010}$ or both, which is consistent with all experimental observations [5,22–24] made so far.

3D nature of magnetism in $GdRu_2Si_2$ *and role of* $\mathbf{Q}_{111}$. The two in-plane vectors $\mathbf{Q}_{100}$ and $\mathbf{Q}_{010}$ have been considered important entities to characterize and understand the magnetic phases of $GdRu_2Si_2$. The obvious reason is that the spin configurations corresponding to different magnetic phases appear and have been observed within the 2D plane of the Gd square lattice. This, together with the layered type structure of $GdRu_2Si_2$ creates an impression of a 2D magnetic system. The interlayer coupling between the Gd layers was also considered weakly FM [21] having no major role in the magnetic properties. Our calculations, however, suggest that this is not true as we find the FM interlayer exchange to be the strongest magnetic interaction in the system, even

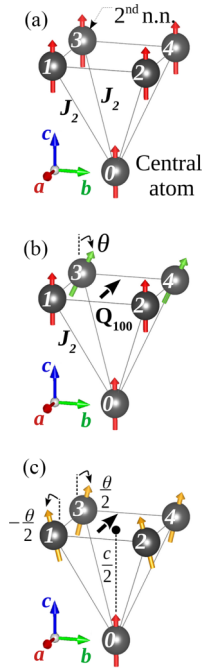


FIG. 4. (a) The central Gd atom from the unit cell origin and its four second nearest neighbors (n.n.) along the [111] directions on the top Gd layer with an FM coupling due to the exchange J_2. (b) A phase difference θ between the four Gd spins on the top layer along the a axis in a helical phase due to the presence of the modulation vector $\mathbf{Q}_{100}$. (c) The same helical phase but with a slightly different spin configuration on the top layer.

stronger than the nearest-neighbor intralayer AFM couplings, which means that $GdRu_2Si_2$ is essentially a 3D magnet. This, together with the *bct* sublattice of the Gd atoms, makes the magnetic phases much more complex than they appear to be with interlayer magnetic coupling and spin-spin correlations. This interlayer correlation could be understood from the following discussion on the role of the strongest FM exchange between layers J_2 in any possible spin spiral state of the system. In this regard, we recall that the zero-field ground state was initially reported to be a helical spiral [5] with a single modulation vector $\mathbf{Q}_{100}$, but more recent experiments have revealed a double-$\mathbf{Q}$ modulated state [22–24] with both $\mathbf{Q}_{100}$ and $\mathbf{Q}_{010}$. For simplicity of analysis, in order to show the importance of the interlayer J_2 exchange coupling, we consider a single-$\mathbf{Q}$ helical state as a reference state here. However, this analysis and the conclusions drawn are valid for any single or double-$\mathbf{Q}$ reference state. Figure 4(a) shows the central Gd atom (zeroth) from the unit cell origin and its four second nearest neighbors (1 to 4) in the next Gd layer forming the square lattice. An FM ordering between the zeroth atom and its four second nearest neighbors is shown considering the ferromagnetic J_2 interaction only. This is true only in the absence of intralayer exchange, which should otherwise induce a spiral ground state. Assuming this state to be a helical state with a single modulation vector $\mathbf{Q}_{100}$, the four spins on the top layer in Fig. 4(a) cannot remain in phase as shown in Fig. 4(b). A phase difference of $\theta = \mathbf{Q_{100}} \cdot \mathbf{a}$ in the third and forth spins with respect to the first and second spins results from the $\mathbf{Q}_{100}$ modulation. Due to this, it is evident that the zeroth spin cannot remain in phase with the four spins on the top layer simultaneously. From Fig. 4(b), we can see that if it stays in phase with the first and second spins, a phase difference of θ must occur with the third and forth spins. The helical state shown in Fig. 4(b) can also be realized with a slightly different spin configuration as depicted in Fig. 4(c). If we ignore the zeroth spin and J_2 exchange coupling, then both Figs. 4(b) and 4(c) represent the same magnetic state (helical state) on the top layer and are energetically degenerate. In both cases, the phase difference between two neighboring spins along $\mathbf{a}$ is θ due to $\mathbf{Q}_{100}$. However, if we consider the interlayer interaction J_2 with the zeroth spin, then the configuration in Fig. 4(c) shall become energetically more favorable over the configuration in Fig. 4(b). This can be seen from the energy differences between the spin configurations in Figs. 4(a)–4(c). If we consider unit spins on the Gd atoms, then the energy difference between configurations (b) and (a) is $E_b - E_a = 4J_2(1 - \cos^2(\theta/2))$, whereas for the configurations (c) and (a) $E_c - E_a = 4J_2(1 - \cos(\theta/2))$. Now, for any small value of the spin canting angle θ, $\cos^2(\theta/2) < \cos(\theta/2)$, and hence $E_c < E_b$. So the spiral spin configuration in Fig. 4(c) is energetically preferable.

This analysis shows an important spin correlation between the second neighbor spins along the body diagonal direction $(\mathbf{a}+\mathbf{b}+\mathbf{c})$ or [111]. If we have an intralayer phase difference of θ between two neighbors along $\mathbf{a}$ or $\mathbf{b}$ due to $\mathbf{Q}_{100}$ or $\mathbf{Q}_{010}$, then an interlayer phase difference of $\theta/2$ must occur between two neighboring spins along $(\mathbf{a}+\mathbf{b}+\mathbf{c})$ having a distance of $|\mathbf{a}+\mathbf{b}+\mathbf{c}|/2$ between them. As a result, the phase difference between the second neighbors along the $(\mathbf{a}+\mathbf{b}+\mathbf{c})$ direction with a distance of $|\mathbf{a}+\mathbf{b}+\mathbf{c}|$ between them should be θ. Hence, in a spiral state described by IP modulation vectors $\mathbf{Q}_{100}$ or $\mathbf{Q}_{010}$ or both, with a corresponding wavelength of λ, there shall be another modulation vector $\mathbf{Q}_{111}$ along $(\mathbf{a}+\mathbf{b}+\mathbf{c})$ with the same wavelength λ but in units of $(\mathbf{a}+\mathbf{b}+\mathbf{c})$. The presence of $\mathbf{Q}_{111}$ as a spiral modulation vector is also evident in the FT $J(q)$ along the *G-A* direction shown in Fig. S4 (d). *G-A* is near $\parallel$ to the [111] direction and $J(q)$ shows a spiral stability. However, the confirmation comes from our ASD simulations, as discussed in the next section. Note that $\mathbf{Q}_{111}$ cannot be ignored and defines the magnetic phases in $GdRu_2Si_2$ together with $\mathbf{Q}_{100}$ and $\mathbf{Q}_{010}$. This happens because of the 3D nature of the magnetic properties of the system, which must be taken into account when doing the ASD simulations. If we consider a simulation cell with the generalized dimension $N_1 \times N_2 \times N_3$, then the presence of two in-plane vectors $\mathbf{Q}_{100}$ and $\mathbf{Q}_{010}$ requires (i) $N_1 = N_2 = m$ where m is some integer. However, the presence of $\mathbf{Q}_{111}$ along with $\mathbf{Q}_{100}$ and $\mathbf{Q}_{010}$ requires (ii) $N_1 = N_1 = N_3 = m$ for $GdRu_2Si_2$ as an essential condition. Deviating from the second condition will make the ASD simulation fail to stabilize a proper spin spiral characterized by the IP vectors $\mathbf{Q}_{100}$ and $\mathbf{Q}_{010}$.

2. *ASD simulations to confirm the presence of* $\mathbf{Q}_{111}$

Some technical considerations for ASD simulations. Before presenting the results from our ASD simulations to confirm the presence of $\mathbf{Q}_{111}$ and the 3D nature of magnetism in $GdRu_2Si_2$, we briefly want to discuss some technical aspects of accurately performing these simulations. This approach to the ASD simulation can be applied to many other noncollinear

TABLE I. Integer ($n = 1$ to 10) multiple of the theoretically obtained in-plane spiral wavelength λ_{100} and the closest simulation cell dimensions ($m \times m \times m$) that can accommodate this spin spiral. A mismatch between the cell dimensions and the spiral wavelength is shown as well, calculated as $\frac{n\lambda_{100}-m\cdot a}{n\lambda_{100}} \times 100\%$, to characterize how optimal the choice of the simulation cell is.

$Q_{100} = (0.19, 0, 0)\frac{2\pi}{a}$; $\lambda_{100} = 5.26$a			
n	$n \times \frac{\lambda_{100}}{a}$	integer 'm'	Mismatch
1	5.26	5	4.9%
2	10.52	11	4.6%
3	15.78	16	1.4%
4	21.04	21	0.2%
5	26.30	26	1.1%
6	31.56	32	1.4%
7	36.82	37	0.5%
8	42.08	42	0.2%
9	47.34	47	0.7%
10	52.60	53	0.8%

magnets with spiral or skyrmion phases and could be very helpful. From our calculated exchange, we get a modulation vector of $\mathbf{Q}_{100} = (0.19, 0, 0)$ in units of $|\mathbf{a}^*| = 2\pi/a$. This suggests an in-plane periodicity or wavelength of $\lambda_{100} = 5.26a$ along **a** corresponding to the resulting exchange spiral, which is incommensurate with the lattice periodicity. However, an integer multiple of λ_{100}, $(n \times \lambda_{100})$ could become close to $(m \times a)$ and be almost lattice-commensurate for some values of n, where n and m are integers. This information is important for choosing the size of the simulation cell ($m \times m \times m$) in ASD calculation and is provided in Table I for reference. From Table I, we can see that any arbitrary value of m will not be able to accommodate an integer number of wavelengths of spiral states. As a result, for the best outcome from the ASD simulation, the values of m reported in Table I, and as large as possible, shall be considered to satisfy the dimensional condition $N_1 = N_1 = N_3 = m$ for $GdRu_2Si_2$. Among these "recommended" integer m values, some of them might be preferable, based on how well the condition $(n \times \lambda_{100}) \approx (m \times a)$ is satisfied. This can be characterized by the mismatch $\frac{n\lambda_{100}-m\cdot a}{n\lambda_{100}} \times 100\%$, which is also shown in Table I for different m values. These considerations become crucial for this system, as the exchange interactions are quite weak and frustrated. A larger deviation from the calculated values of m acts as a perturbation and can distort the spiral states. Such a distortion due to unpreferred values of m is, however, different from the major destabilization resulting from violating the essential condition $N_1 = N_1 = N_3 = m$ for $GdRu_2Si_2$.

Confirmation of the 3D nature and $\mathbf{Q}_{111}$. To check if our reasoning is correct, we performed ASD simulations with three different simulation cells having dimensions $37 \times 37 \times 37$, $37 \times 37 \times 21$, and $37 \times 37 \times 3$ respectively at $H = 0$ T and $T = 0$ K. Note that in these simulations, we modify only one dimension of the simulation cell, while the rest of the computational parameters and the spin Hamiltonian remain the same. The first cell satisfies condition $N_1 = N_1 = N_3 = m$ with $m = 37$ from Table I and should stabilize a pure (defect-free) spiral state. In contrast, the second and third are expected

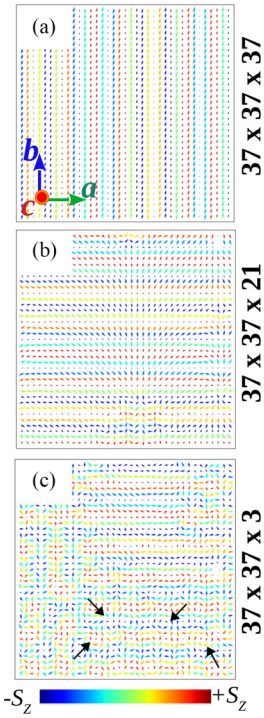


FIG. 5. Spin configuration after ASD simulations, of the top Gd layer of the simulation cell with dimension (a) $37 \times 37 \times 37$, (b) $37 \times 37 \times 21$, and (c) $37 \times 37 \times 3$, respectively. These ASD simulations were done using a spin Hamiltonian with only exchange (J_{ij}) and uniaxial anisotropy (K_U).

to show additional deformations as we deviate from the $N_1 = N_2 = N_3 = m$ condition. In the second calculation, we do this by choosing $N_3 = 21$, which is also a good number from Table I to accommodate an integer number of spiral wavelengths but is $< N_1, N_2$. In the third calculation, we set $N_3 = 3$, which is less than 5, the minimum value required to accommodate a single wavelength. In this case, we expect a complete failure of the ASD simulation to stabilize a proper spiral state. In these ASD simulations, the exchange interactions (J_{ij}) and a uniaxial anisotropy energy (K_U) of $\sim$0.05 meV along the out-of-place **c** axis were considered in the spin Hamiltonian [see Eq. (5)]. K_U was calculated from DFT following a method described in detail in the methodology section. The value is in agreement with the one reported in recent literature [41]. The spin configuration of the upper Gd layer of the simulation cell from the three calculations is presented in Fig. 5. The simulation cell of dimension $37 \times 37 \times 37$ can stabilize a defect-free helical spiral with $\mathbf{Q}_{100}$ as shown in Fig. 5(a). This helical phase was initially reported as the ground state of $GdRu_2Si_2$ [5] but more recent experiments [22–24] have found a different spiral state with a double-**Q** modulation. This discrepancy could be ignored at the moment as the primary purpose of our current calculation is to obtain a defect-free spiral state resulting mainly from exchange frustration. The nature of the spiral will change based on additional interactions, e.g., magnetocrystalline anisotropy, in the Hamiltonian. The stabilization of the correct ground state will be addressed in more detail in the next section. The $37 \times 37 \times 21$ simulation cell still produces a helical state

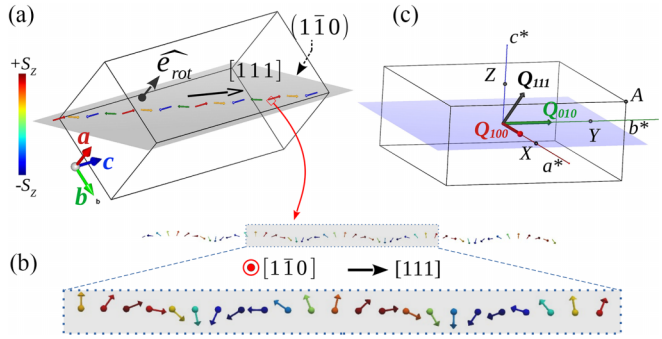


FIG. 6. (a) The presence of a spin spiral in the atomic chain along the [111] direction in the spiral state where the spins in the 2D (001) planes form a helix along the [100] direction [see Fig. 5(a)]. (b) Cycloidal nature of the interlayer spiral along [111] with a spiral rotation vector along [1$\bar{1}$0]. (c) A schematic representation of the Brillouin Zone, illustrating the orientation of the **Q**-vectors $\mathbf{Q}_{100}$, $\mathbf{Q}_{010}$, and $\mathbf{Q}_{111}$. The high-symmetry points X, Y, Z, and A are also marked for reference.

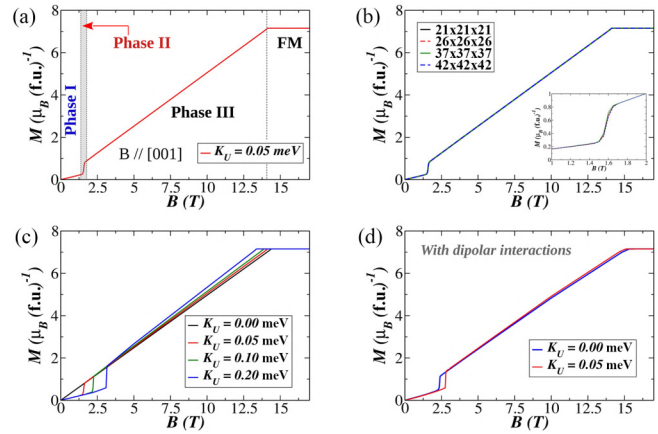


FIG. 7. (a) Theoretically computed M vs B data for $K_{\mathrm{U}} = 0.05$ meV and using a $37 \times 37 \times 37$ simulation cell, showing the presence of three different phases before the FM phase similar to the experimental report [5]. (b) Comparison of calculated M vs B data with different simulation cell sizes. $K_{\mathrm{U}} = 0.05$ meV was used in these calculations. The inset shows a magnified version of the phase II region. (c) $M(B)$ curves for different anisotropy constants showing the importance of K_{U}. A $37 \times 37 \times 37$ simulation cell was used here. (d) $M(B)$ curves in the presence of dipolar interactions with and without anisotropy constants (where a $21 \times 21 \times 21$ simulation cell was used).

defined by a $\mathbf{Q}_{010}$ but with additional distortions as shown in Fig. 5(b). The simulation cell $37 \times 37 \times 3$ cannot reproduce the helical state or any proper spin state that can be described by the IP **Q**-vectors as shown in Fig. 5(c). Instead, we observe a mixed disordered spin state with some isolated skyrmionlike spin vortices marked by small black arrows. This result is interesting because it opens up a new avenue to stabilize a skyrmion configuration outside of the common approach of applying an external magnetic field. Hence, this observation could be exploited to stabilize skyrmion textures in magnetic films, including the skyrmion lattice.

Characterization of the $\mathbf{Q}_{111}$ *spiral.* Finally, in Fig. 6, we show the arrangements of the spins in the atomic chain along the $(\mathbf{a}+\mathbf{b}+\mathbf{c})$ or [111] direction in the proper helical phase coming from the $37 \times 37 \times 37$ cell simulation shown in Fig. 5(a). The spin arrangements clearly show a cycloidal-type spin-spiral as shown in Fig. 6(b), propagating along the [111] direction, confirming the presence of the $\mathbf{Q}_{111}$ modulation vector and 3D magnetism in $GdRu_2Si_2$. In this cycloidal spiral, the spins lie mainly in the (1$\bar{1}$0) plane and rotate about to the spiral rotation direction $\hat{e}_{\mathrm{rot}}$ nearly parallel to the [1$\bar{1}$0] direction as shown schematically in Fig. 6(a). For a clearer understanding of the spin-spiral vectors, Fig. 6(c) presents a schematic of the Brillouin zone. This diagram illustrates the orientation of $\mathbf{Q}_{111}$ relative to $\mathbf{Q}_{100}$ and $\mathbf{Q}_{010}$. The magnitudes of the vectors are slightly exaggerated for visual clarity. It is important to note that $\mathbf{Q}_{111}$ is not parallel to the Γ-A high-symmetry direction. The nature of this spiral along [111] will also change when the present helical phase of the system changes to a different phase. However, $\mathbf{Q}_{111}$ and an associated spiral will always persist because of interlayer exchange coupling.

To show the robustness and presence of $\mathbf{Q}_{111}$ in any spiral phase, we show in Fig. 7(a) the simulated magnetic response [magnetization (M) versus magnetic field (B) measurements]. To obtain this $M(B)$ curve, a Zeeman term in the spin Hamiltonian [Eq. (5)] was considered along with exchange (J_{ij}) and anisotropy (K_{U}). The ASD simulations were then performed for a range of external field values applied along the c axis at zero temperature with the same simulation cell $37 \times 37 \times 37$. We obtain excellent qualitative agreement showing the presence of three distinct phases before entering the fully polarized FM phase, similar to that in the experiment [5]. This establishes the physical validity of our calculated J_{ij} and K_{U} on strong ground and shows the reliability of the methods used here. The $\mathbf{Q}_{111}$ and interlayer spin-spin correlation also remains in B induced phases II and III. The cycloid along [111] shown in Fig. 6 from phase I transforms into a helical and conical-type spiral in phases II and III, respectively, with $\hat{e}_{\mathrm{rot}}$ near $\parallel$ [111]. A comparative view of the $\mathbf{Q}_{111}$ spiral in the three phases is shown in Fig. S5 of SM Ref. [46]. We end this discussion with another important observation. The spins along the interlayer [001] direction are coupled ferromagnetically compared to the [111] direction, showing a spin spiral, as discussed above. This happens because the spins along [001] consist of the same type of atoms coupled by J_7, while along [111] we have two different types [see Fig. 1(a)] coupled by J_2.

3. Investigating the magnetic ground state

This section investigates the origin of the fine modulations in the magnetic phases which require interactions beyond exchange and uniaxial anisotropy. We carefully checked the role of (i) simulation cell size, (ii) values of the calculated exchange and uniaxial anisotropy parameters, and (iii) weak magnetic interactions. We show that reproducing the correct magnetic state/spin configuration in each phase requires accurate modeling of the system with weak magnetic interactions. Knowing the zero-field ground state is essential for correctly simulating any temperature/field-induced spin state. For example, although the spin configurations in our simulated phases I, II, and III from Fig. 7(a) are different from each

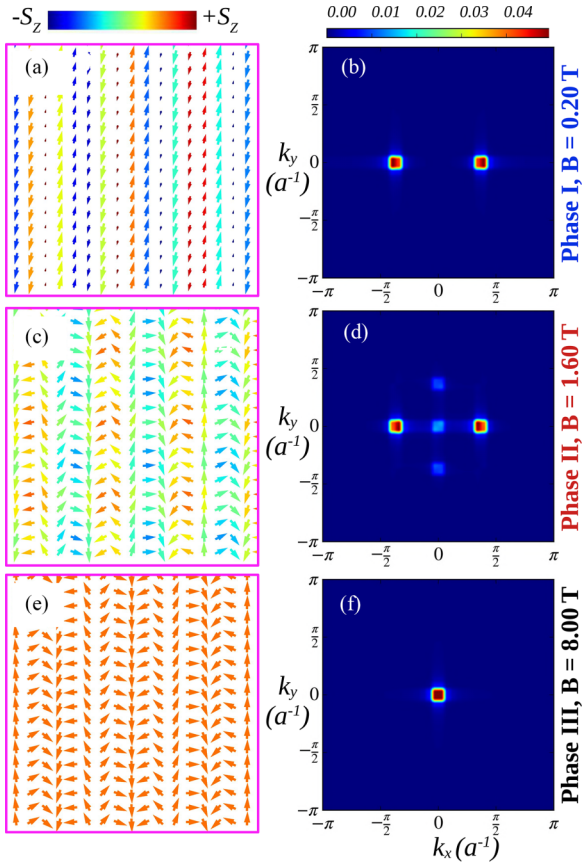


FIG. 8. (Left) Spin configuration within the 2D Gd layers in (a) phase I, (c) phase II, and (e) phase III, respectively, after the ASD simulation with $K_U = 0.05$ meV, same as in Fig. 7(a). A $17 \times 17 \times 1$ square was cut from the $37 \times 37 \times 1$ plane for a better view of the arrangements. (Right) The out-of-plane (OP) spin structure factor (S_s^{OP}) for (b) phase I, (d) phase II, and (f) phase III, respectively. See the text for details.

other, they are not the ones experimentally observed. This is not surprising because our simulation, as discussed earlier, failed to stabilize the correct ground state. Figures 8(a), 8(c), and 8(e) show the spin configurations of phases I, II, and III, respectively, from our ASD simulations. The difference could easily be verified with the **Q** vectors in the calculated spin structure factor, the methodology of which is described in Sec. VI of SM Ref. [46]. The out-of-plane (OP) spin-structure factor corresponding to the three phases is shown in Figs. 8(b), 8(d), and 8(f), respectively. The in-plane (IP) spin-structure factor of all three phases is identical, showing a single-**Q** modulation, and is not shown in the main text (see Fig. S6 of SM Ref. [46] for the IP structure factors). Phase I is the helical state (similar to our zero-field ground state) with a single **Q** modulation and is not the correct one according to recent experiments. This state was initially reported as the zero-field ground state by N. D. Khanh *et al.* [5]. However, a double-**Q** state was later identified from resonant x-ray scattering experiments with polarization analysis [22]. The spin configuration of this state was represented by an orthogonal superposition of a proper screw spiral and a sinusoidal wave [22,66]. The IP spin structure factor of this state shows a double-**Q** modulation with different intensities that leads to a periodic array of vortices [66]. However, the OP structure factor shows a single-**Q** modulation. The double-**Q** ground state of $GdRu_2Si_2$ was also recently confirmed by neutron diffraction measurement [23] and spin-polarized scanning tunneling microscopy [24]. Returning to our results, in phase III, we get FM-ordered S_z spin components and single-**Q** xy components, suggesting a conical spiral state, but recent experiments report a Meron-like crystal/lattice here [22,23]. Our calculated phase II shows double-**Q** modulated S_z spin components with different intensities along two directions [Fig. 8(d)], but it is not the experimentally reported and most discussed SkL phase. The difference between the three phases in Fig. 8 could also be realized more easily from the real space spin-density distribution of the z component of the spin density and is discussed in Sec. VIII of SM Ref. [46].

(i) *Verification of simulation parameters.* Hence, we now focus on the reason that causes a destabilization of the correct zero-field double-**Q** ground state in our ASD simulations. (A) First, we check whether the simulation cell size $37 \times 37 \times 37$ is sufficient to capture the fine details of the magnetic configurations in each phase. For this, we consider a larger cell $42 \times 42 \times 42$ with $m = 42$ from Table I. As can be seen, this also has a lower % mismatch and is expected to give better results. We have also considered two lower-dimensional cells $21 \times 21 \times 21$ and $26 \times 26 \times 26$ with $m = 21$ and 26 respectively from Table I for a better comparison. The $M(B)$ curves obtained from the ASD simulations using simulation cells of different sizes are shown in Fig. 7(b). The same computational settings and spin Hamiltonian were used in these calculations that we used before for $37 \times 37 \times 37$. We see an excellent outcome with all the curves overlapping with each other. For a better view, a magnification of the transition regions around phase II is shown in the inset of Fig. 7(b). We also confirm that the spin configurations in the three phases and the ground state of the four $M(B)$ curves in Fig. 7(b) are similar. We have shown these states of the $42 \times 42 \times 42$ cell in Fig. S8 of SM Ref. [46] to compare with the $37 \times 37 \times 37$ ones shown in Fig. 8. So, the values of $m \geqslant 20$ in Table I are almost equally good for a simulation cell and do not lead to incorrect spin configurations. (B) Second, we review exchange interactions from an accuracy point of view. As discussed in the last section, the soundness of our exchange parameters is undeniable from their efficiency in describing the magnetic phase transitions in Fig. 7(a). However, all methodologies used to calculate exchange interactions will have some inaccuracies. For example, the values of the exchange parameters calculated using a different method or a different software could differ slightly from the ones we have [as shown in Fig. 3(a)]. To check if this has anything to do with the magnetic ground state, we calculated the first three exchange parameters J_1, J_2, and J_3 using the total energy method. A detailed description of this method and the calculation process is given in Sec. X of SM Ref. [46]. RSPT, as well as VASP, was used for this purpose, and the calculated values are shown in Table II comparatively along with the MFT calculated values from Fig. 3(a).

We obtain a good agreement between the RSPT and VASP total energy calculations, which is a good sign since we are using the same method here. However, these values do not fully agree with the MFT-calculated values of J_1, J_2, and

TABLE II. Calculated values of the exchange parameters J_1, J_2, and J_3 using the total energy method in RSPT and VASP. The MFT calculated values from Fig. 3(a) are also tabulated for comparison purposes.

Calculation method	Exchange parameter values (mRy)		
	J_1	J_2	J_3
Total energy method in VASP	0.025	0.086	−0.009
Total energy method in RSPT	0.018	0.081	−0.011
Magnetic force theorem in RSPT	−0.004	0.095	−0.012

J_3. Although J_2 and J_3 are all very similar, J_1 in the total energy calculations is noticeably larger and also FM in nature compared to its weak AFM counterpart from the MFT calculation. This could indeed alter the nature of the zero-field ground state and this was investigated. Since the total energy calculated values from RSPT and VASP are very close, only the VASP calculated values were considered for this check. First, to check the dominant **Q** vectors in this case, the MFT calculated J_1, J_2, and J_3 in our J_{ij}s were replaced with the VASP calculated values from Table II. Then FT $J(q)$ was calculated for $\mathbf{q} \parallel$ different directions of the Brillouin zone and are shown in Fig. S10 of SM Ref. [46]. The results are qualitatively the same as before with $\mathbf{Q}_{100}$ and $\mathbf{Q}_{010}$ showing maximum stability over other spiral modulation vectors. In this case, we get $|\mathbf{Q}_{100}| = |\mathbf{Q}_{010}| = 0.18\mathbf{a}^*$, slightly less than $0.19\mathbf{a}^*$ obtained before with all MFT calculated values of J_{ij}s. Hence, we can expect a very similar helical spiral ground state from here also. To confirm this, a $(B, T) = 0$ ASD simulation was performed with this new set of exchange parameters and $K_U = 0.05$ meV. The helical spin state in the 2D Gd layer and its characterization from the IP and OP spin structure factor are shown in Fig. S11 of SM Ref. [46]. This analysis suggests that as long as we obtain the stabilization of $\mathbf{Q}_{100}$ and $\mathbf{Q}_{010}$ from some exchange parameters (J_{ij}), an ASD simulation along with some K_U would possibly stabilize some single-**Q** ground state. Small deviations/inaccuracies in calculated J_{ij}s that come from different calculation methods should not make any difference and cannot be a reason for missing the correct double-**Q** ground state. This statement is also supported by the data presented in a recent work by Bouaziz *et al.* [21] where ASD simulation with their J_{ij}s showing the same $\mathbf{Q}_{100}$ stability and K_U resulted in the same helical ground state that is presented here. Hence, for any further calculations and analysis, we stick to our MFT calculated exchange parameters in Fig. 3(a). (C) Third, we have to discuss the role of uniaxial anisotropy K_U. As our ASD simulations are using the DFT calculated anisotropy value of $K_U = 0.05$ meV, a number that might have uncertainty in it, the influence of the magnetic anisotropy on the magnetic configuration also needs to be checked. The simulated $M(B)$ curves for different values of K_U are shown in Fig. 7(c). For these calculations, we used the same $37 \times 37 \times 37$ simulation cell, and all other computational settings were kept fixed. An increased anisotropy value of 0.10 meV gives a much better description of the magnetic response (green curve). Phase II now appears around the experimental value of $B = 2.00$ T compared to the $K_U = 0.05$ meV case that shows it around 1.50 T. However, even with this improvement, the spin configurations in each phase, including the zero-field ground state, do not change. All come out to be the same as before, along with the same helical state at zero-field. The spin configurations and the corresponding spin structure factors of these phases are shown in Fig. S12 of SM Ref. [46]. For a deeper understanding of the role of K_U, it was removed from a set of ASD simulations to see the effect on the $M(B)$ curve. This gives a dramatic outcome where exchange alone fails to predict the known magnetic phase transitions (black curve). The system directly enters the field-polarized FM state from the only observed conical spiral state. This observation emphasizes the importance of K_U in $GdRu_2Si_2$. This also aligns with the study of Bouaziz *et al.* [21], where a large value of K_U around 0.30 meV was reported to have been used in the ASD simulations to stabilize a SkL phase under an applied magnetic field. Following Ref. [21], we further increased the value of K_U to 0.20 meV. This affected the $M(B)$ curve, pushing phase II even higher along the B axis, but the nature of the phases did not change (data not shown here). With larger K_U values, Bouaziz *et al.* [21] also reports the same zero-field helical spiral ground state and a high-field conical spiral state similar to our results, contradicting the recent experimental data [22–24]. However, their calculation surprisingly shows a SkL state for some critical values of the B field. One possible reason for this stabilization could be the $60 \times 60 \times 6$ simulation cell used in their calculation, deviating from the $N_1 = N_2 = N_3$ condition we propose for this system. We have already shown in the previous section [Fig. 5(c)] that such a cell could induce skyrmion-like objects even at $B = 0$T. Hence, a simulation cell of this kind, along with K_U around 0.30 meV, could stabilize a SkL state as was claimed [21]. However, considering the 3D nature of magnetism in $GdRu_2Si_2$, the SkL state reported in Ref. [21] could be a special case. Hence, from here we can conclude that K_U is essential to correctly describe the magnetic phase transitions of $GdRu_2Si_2$, but not a sufficient element to stabilize the correct spin states or the double-**Q** ground state.

(ii) *Critical role of dipolar interactions.* Lastly, we want to discuss the role of weak magnetic interactions not considered in our spin Hamiltonian. The microscopic magnetic interactions we have been considering are the isotropic Heisenberg exchange (bilinear) and uniaxial anisotropy. Although the on-site uniaxial anisotropy (K_U) cannot change the single-**Q** helical ground state, some other inter-site interactions like exchange could. In this regard, weak magnetic interactions such as the biquadratic interaction, dipolar interaction, and symmetric anisotropic exchange (SAE) interaction could play an important role. A complete understanding will need to consider each of these weak interactions separately and their all possible combinations with exchange (J_{ij}) and anisotropy (K_U). This is going to be a separate study on its own and is beyond the scope of our present work. However, among the three interactions mentioned, the magnetic dipolar interaction should not be ignored. Magnetic dipolar interactions are naturally present in any magnetic material and could become important in a system like $GdRu_2Si_2$, where large atomic moments of $7.0\mu_B$ are present, potentially leading to non-negligible dipolar interactions, especially compared

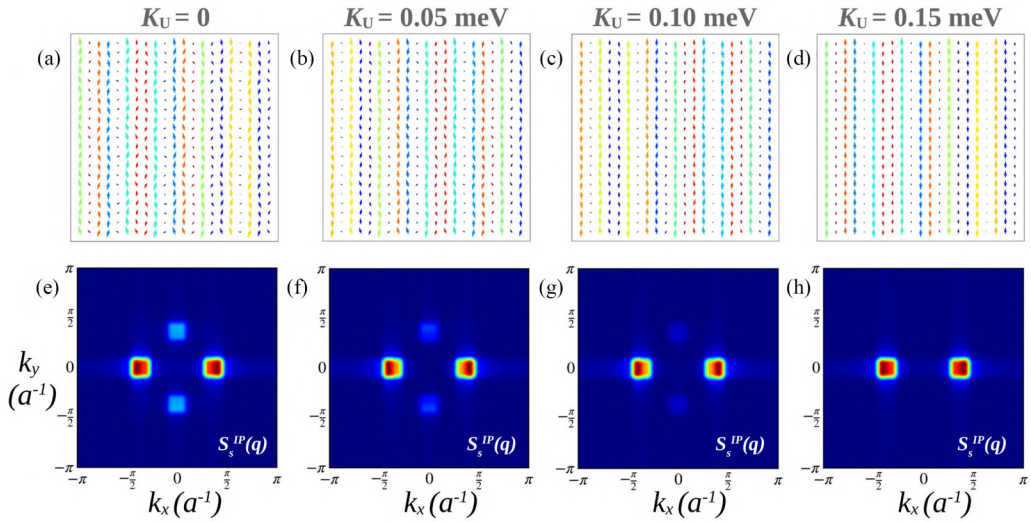


FIG. 9. Effect of uniaxial anisotropy K_U in the presence of dipolar interactions. (Top) Spin configuration within the $21 \times 21 \times 1$ 2D Gd layers for (a) $K_U = 0$, (b) 0.05, (c) 0.10, and (d) 0.15 meV respectively. (Bottom) The corresponding IP spin structure factor (S_s^{IP}) of the spin states shown in the top panel. See the text for more details.

to relatively small Heisenberg interactions [Fig. 3(a)]. The role of dipolar exchange in stabilizing topological magnetic structures like magnetic bubbles or skyrmions is well known from previous studies of similar systems [67–69]. Hence, we now add the dipolar interaction term defined in Eq. 6 within our spin Hamiltonian in Eq. (5) with exchange, uniaxial anisotropy, and the Zeeman term for ASD simulations. The inclusion of dipolar interactions makes the ASD simulations computationally very demanding.

To reduce the computational load, we used the simulation cell $21 \times 21 \times 21$, with a tetragonal shape, which is equally accurate as the $37 \times 37 \times 37$ cell, as discussed at the very beginning of this section [Fig. 7(b)]. In the previous paragraph, we have also discussed the importance of on-site uniaxial anisotropy (K_U) for a correct description of the magnetic phase transitions in $GdRu_2Si_2$ [Fig. 7(c)]. For this reason, we perform $(B, T) = 0$ ASD simulations with dipolar interactions and for different values of K_U to check the possible ground-state structures. The spin configurations in the 2D Gd layers of the resulting ground states are shown in the top panel of Fig. 9, and the bottom panel shows the corresponding IP spin structure factors. The OP spin structure factor for all the cases shows similar single-**Q** modulation of the spins and is not shown here in the main text (see Fig. S13 of SM Ref. [46] for the OP case). For $K_U = 0.15$ meV, we get a perfect helical spiral with a single-**Q** modulation. As the value of K_U is decreased, the spins start to show some planar rotations, which become very pronounced in the form of some vortices when K_U is removed. This is not a helical spiral state, and it is clear from the IP spin structure factor showing a double-**Q** modulation with different intensities along the two in-plane directions. Such rotational behavior of the in-plane components of the spins and the corresponding double-**Q** structure factor in Figs. 9(a) and 9(e), respectively, matches with the experimentally reported double-**Q** ground state [22–24]. Our simulated ground state is in excellent qualitative agreement with experimental reports. The minor quantitative difference observed in the spin rotation amplitude is an expected outcome of comparing first-principles calculations with experimental observations and does not alter our fundamental physical conclusions. These results show the importance of dipolar interactions for the correct ground state properties of the system. This spiral state persists for our DFT calculated value of $K_U = 0.05$ meV, but with a lower intensity and almost dissipates above this value. For $K_U = 0.15$ meV, on-site uniaxial anisotropy dominates over dipolar interactions, stabilizing the helical spiral state again. This observation is, however, not surprising but more realistic because a small value of K_U is something to expect in $GdRu_2Si_2$. In $GdRu_2Si_2$, Gd^{3+} cations with $S = 7/2$ and $L = 0$ are expected to show a very small or zero value of K_U due to the zero orbital moment in this case [70]. To understand the importance of K_U in the presence of dipolar interactions, we again calculate the $M(B)$ curve without any K_U (blue line) as shown in Fig. 7(d). Interestingly, we get an excellent qualitative description of the magnetic transitions showing all three phases even without K_U. Phase II also appears around the experimental value of $B = 2.0\,T$. This is strikingly different from the data without dipolar interactions [see Fig. 7(c)], where K_U was essential to simulate the magnetic response of the system correctly. Since we get the correct ground state and magnetic transitions with dipolar interactions and without any K_U, we can anticipate the experimentally reported SkL state in phase II and a Meron-like state in phase III. The spin configurations in the three phases and their characterization with the spin structure factor are given in Fig. S14 of SM Ref. [46]. Phases II and III do not show a SkL and Meron-like lattice but are very similar to what we got before without dipolar interactions (Fig. 8). One reason behind the absence of a SkL and Meron-like lattice in phases II and III could be the exclusion of K_U from these calculations. Although in the presence of dipolar interactions K_U looks a bit irrelevant, a small value could be important for any B-induced spin states. To check this, the $M(B)$ curve was calculated with our DFT calculated value of $K_U = 0.05$ meV (red line) and is also shown in Fig. 7(d). Phase II is again pushed higher in the B axis as expected but no other changes in the spin

configurations of any phases were observed. We get the same spin states in the three phases observed earlier for the $K_U = 0$ case (data not shown here). From Fig. 9, we already know that a larger value of K_U destabilizes the correct ground state properties and hence should not be used aiming to stabilize a SkL state in phase II or a Meron-like configuration in phase III. For this reason and due to the demanding nature of these dipolar calculations, we have not calculated the $M(B)$ curves for any larger K_U values. Our results show the importance of dipolar interactions in $GdRu_2Si_2$ for obtaining the correct magnetic ground state and also play a similar role like the uniaxial anisotropy to control the magnetic phase transitions.

(iii) *Path to a complete microscopic description.* Our data also suggest that other weak interactions, such as the biquadratic interaction and symmetric anisotropic exchange interaction, may be crucial for stabilizing the correct field-induced spin states. For a symmetric tetragonal crystal like this, the importance of biquadratic interaction mediated by itinerant electrons in the presence of an easy axis anisotropy to stabilize a multiple-**Q** SkL state over a single-**Q** spiral state has been claimed before [5,22,66]. In this regard, the theoretical work by Hayami *et al.* [66] is particularly noteworthy. They considered a model Hamiltonian based on a Kondo lattice model consisting of itinerant electrons and localized spins. The Hamiltonian included both bilinear and biquadratic interactions, and its role was analyzed for a two-dimensional square lattice. The biquadratic exchange interaction was found to be important in stabilizing any spin state with a double-**Q** modulation, which could be further stabilized by bond-dependent anisotropic interactions. Such states could transform into a proper SkL state with the application of an external magnetic field. While Hayami's study is based on a two-dimensional square lattice, which deviates from our finding that $GdRu_2Si_2$ is a three-dimensional magnet, it is impressive that their model manages to reproduce the experimentally observed phase diagram. The findings on the importance of specific physical interactions, therefore, remain scientifically valuable and strongly suggest a reason for our simulations' inability to stabilize the field-induced SkL state. However, our computational approach is based on the first principles, where all microscopic interactions are derived from DFT data. Calculating biquadratic interactions from DFT is a significant methodological challenge that requires new implementations and rigorous tests on known systems and is beyond the scope of this work.

Despite this constraint, the value of our methodology and the results obtained so far are important. Our simulations use a Hamiltonian built upon parameters derived directly from first-principles density functional theory, an approach that avoids parameter fitting. This provides a realistic and physically grounded starting point for achieving a microscopic understanding of any magnetic system. The value of this methodology is that it systematically reveals which microscopic interactions are essential for accurately reproducing experimental observations. Although our simulations here do not stabilize the most-discussed field-induced SkL state, they correctly capture the zero-field double-**Q** ground state and the overall magnetic phase transitions. This provides a crucial foundation for future work. By systematically building upon our DFT-derived Hamiltonian, one could meticulously investigate the effects of additional weak interactions like biquadratic exchange, as suggested by Hayami *et al.* [66], to eventually reproduce all experimentally observed magnetic phases. We believe that this systematic approach represents a more accurate path toward a comprehensive, first-principles understanding of magnetism in $GdRu_2Si_2$.

IV. CONCLUSION

$GdRu_2Si_2$ is a metallic magnet with Gd $4f$ moments interacting via the RKKY exchange mechanism. This triggers an exchange frustration in the system leading to noncollinearity even without any DMI. Our calculated exchange interactions confirm the RKKY behavior, and the main source of exchange frustration is the competition between the interlayer and intralayer exchange couplings, which are dominantly FM and AFM in nature, respectively. Interestingly, the interlayer FM exchange is much stronger compared to the intralayer AFM interactions, suggesting that $GdRu_2Si_2$ is a 3D bulk magnet, despite its layered-type appearance. With further analysis of the exchange data, we can identify the presence of a previously unnoticed interlayer modulation vector $\mathbf{Q}_{111}$ that coexists with the modulation vectors $\mathbf{Q}_{100}$ and $\mathbf{Q}_{010}$, known from the literature. We could confirm the $\mathbf{Q}_{111}$-modulation of the spin texture in the spiral phases from our spin-dynamics simulations and show that it is in line with its magnetic properties. This interlayer modulation vector cannot be ignored and describes the magnetic phases together with the experimentally observed intralayer modulation vectors $\mathbf{Q}_{100}$ and $\mathbf{Q}_{010}$. This makes the magnetic phases of $GdRu_2Si_2$ far more complex than they appear on the 2D Gd layers, where the interlayer spin correlation results in a complex modulation of the spins. By taking these correlations into account, our spin dynamics simulations can reproduce the magnetic-field-induced phase transitions, in good qualitative agreement with the experimental data. We also demonstrate the importance of dipolar interactions in governing the ground-state magnetic properties of the system. A competition between the effects of dipolar interaction and uniaxial anisotropy was also found, and these two types of interactions attempt to stabilize different magnetic orderings. The dominance of the dipolar interaction over uniaxial anisotropy becomes evident from the ground-state properties. This indirectly points to a weak uniaxial anisotropy consistent with the spherical symmetry of the Gd $4f$ states. However, our simulations are not able to stabilize the experimentally reported SkL and Meron-like states at higher field values. We ascribe this to weak magnetic interactions such as biquadratic and symmetric anisotropic exchange that are absent in our spin Hamiltonian. Nevertheless, our observations so far represent important steps towards a complete understanding of the magnetism of $GdRu_2Si_2$, especially in light of DFT and ASD simulations.

Regarding the computational methodology, we point out the importance of supercell dimensions for modeling the magnetic state using atomistic spin dynamics. Quite different results can be obtained depending on the dimensions, even along the c-axis, relative to the wavelength of the spin spirals and sizes of the skyrmions. This may explain the difference between some of our results and previous studies. This observation can be important for spin dynamics studies of

magnetic systems in general and for noncollinear magnets in particular, where the size effects in terms of the simulation cell dimensions can be of high importance, especially when magnetic textures are not commensurate with the crystal lattice. This also carries over to the experimental investigations in which thin-film growth and/or nanopatterning could be used to induce and manipulate specific skyrmionic states. Further studies and experiments in this direction would potentially provide new insights and advance the field of topological magnetism.

ACKNOWLEDGMENTS

This work was financially supported by the Knut and Alice Wallenberg Foundation through Grants No. 2018.0060, No. 2021.0246, and No. 2022.0108 (PIs: O.E. and A.D.), and R.P. and V.B. acknowledge support from the Göran Gustafsson Foundation (recipient of the "small prize": V.B.). V.B. also acknowledges support by the Swedish Research Council (VR) through Grant No. 2024-05206 and the Ministry of Education, Youth and Sports of the Czech Republic through the e-INFRA CZ (ID:90254). O.E. and A.D. acknowledge support from the Wallenberg Initiative Materials Science for Sustainability (WISE) funded by the Knut and Alice Wallenberg Foundation (KAW). A.D. also acknowledges financial support from the Swedish Research Council (Vetenskapsrådet, VR), Grants No. 2016-05980, No. 2019-05304, and No. 2024-04986. O.E. also acknowledges support by the Swedish Research Council (VR), the Foundation for Strategic Research (SSF), the Swedish Energy Agency (Energimyndigheten), the European Research Council (854843-FASTCORR), eSSENCE and STandUP. S.S. acknowledges funding (postdoctoral stipend) from the Carl Tryggers Foundation (Grant No. CTS 22:2013, PI: V.B.).

The computations/data handling were enabled by resources provided by the Swedish National Infrastructure for Computing (SNIC) at the National Supercomputing Centre (NSC, Tetralith cluster) partially funded by the Swedish Research Council through Grant Agreement No. 2018-05973 and by the National Academic Infrastructure for Supercomputing in Sweden (NAISS) at the National Supercomputing Centre (NSC, Tetralith cluster) partially funded by the Swedish Research Council through Grant Agreement No. 2022-06725. We acknowledge VSB – Technical University of Ostrava, IT4Innovations National Supercomputing Center, Czech Republic, for awarding this project access to the LUMI supercomputer, owned by the EuroHPC Joint Undertaking, hosted by CSC (Finland) and the LUMI consortium through the Ministry of Education, Youth and Sports of the Czech Republic through the e-INFRA CZ (Grant ID: 90254). We also acknowledge EuroHPC Joint Undertaking for awarding us access to Karolina supercomputer at IT4Innovations, Czech Republic. Structural sketches in Figs. 1–4 were produced using the VESTA3 software [71]. Spin configurations in Figs. 5 and 8 were plotted using the SPINVIEW software [72].

We thank Saikat Sarkar (CRIS, India) for useful discussions on this study, Nastaran Salehi and Philipp Rybakov for discussions regarding dipolar exchange and verification of its implementation in the UPPASD software, Manuel Pereiro and Qichen Xu for similar discussions, and Anders Bergman for general discussions about the UPPASD software.

DATA AVAILABILITY

The data that support the findings of this article are not publicly available. The data are available from the authors upon reasonable request.

[1] M. Ślaski, A. Szytuła, J. Leciejewicz, and A. Zygmunt, Magnetic properties of $RERu_2Si_2$ (RE= Pr, Nd, Gd, Tb, Dy, Er) intermetallics, J. Magn. Magn. Mater. **46**, 114 (1984).

[2] M. A. Ruderman and C. Kittel, Indirect exchange coupling of nuclear magnetic moments by conduction electrons, Phys. Rev. **96**, 99 (1954).

[3] I. Dzyaloshinsky, A thermodynamic theory of "weak" ferromagnetism of antiferromagnetics, J. Phys. Chem. Solids **4**, 241 (1958).

[4] T. Moriya, Anisotropic superexchange interaction and weak ferromagnetism, Phys. Rev. **120**, 91 (1960).

[5] N. D. Khanh, T. Nakajima, X. Yu, S. Gao, K. Shibata, M. Hirschberger, Y. Yamasaki, H. Sagayama, H. Nakao, L. Peng *et al.*, Nanometric square skyrmion lattice in a centrosymmetric tetragonal magnet, Nat. Nanotechnol. **15**, 444 (2020).

[6] A. Fert, N. Reyren, and V. Cros, Magnetic skyrmions: advances in physics and potential applications, Nat. Rev. Mater. **2**, 17031 (2017).

[7] S. Seki, M. Garst, J. Waizner, R. Takagi, N. D. Khanh, Y. Okamura, K. Kondou, F. Kagawa, Y. Otani, and Y. Tokura, Propagation dynamics of spin excitations along skyrmion strings, Nat. Commun. **11**, 256 (2020).

[8] A. Neubauer, C. Pfleiderer, B. Binz, A. Rosch, R. Ritz, P. G. Niklowitz, and P. Böni, Topological Hall effect in the a phase of MnSi, Phys. Rev. Lett. **102**, 186602 (2009).

[9] N. Kanazawa, Y. Onose, T. Arima, D. Okuyama, K. Ohoyama, S. Wakimoto, K. Kakurai, S. Ishiwata, and Y. Tokura, Large topological Hall effect in a short-period helimagnet mnge, Phys. Rev. Lett. **106**, 156603 (2011).

[10] Y. Shiomi, N. Kanazawa, K. Shibata, Y. Onose, and Y. Tokura, Topological Nernst effect in a three-dimensional skyrmion-lattice phase, Phys. Rev. B **88**, 064409 (2013).

[11] Y. P. Mizuta and F. Ishii, Large anomalous nernst effect in a skyrmion crystal, Sci. Rep. **6**, 28076 (2016).

[12] A. Fert, V. Cros, and J. Sampaio, Skyrmions on the track, Nat. Nanotechnol. **8**, 152 (2013).

[13] T. Nomoto, T. Koretsune, and R. Arita, Formation mechanism of the helical q structure in Gd-based skyrmion materials, Phys. Rev. Lett. **125**, 117204 (2020).

[14] Y. Ishikawa, K. Tajima, D. Bloch, and M. Roth, Helical spin structure in manganese silicide MnSi, Solid State Commun. **19**, 525 (1976).

[15] S. Mühlbauer, B. Binz, F. Jonietz, C. Pfleiderer, A. Rosch, A. Neubauer, R. Georgii, and P. Böni, Skyrmion lattice in a chiral magnet, Science **323**, 915 (2009).

[16] B. Lebech, J. Bernhard, and T. Freltoft, Magnetic structures of cubic FeGe studied by small-angle neutron scattering, J. Phys.: Condens. Matter **1**, 6105 (1989).

[17] X. Z. Yu, N. Kanazawa, Y. Onose, K. Kimoto, W. Z. Zhang, S. Ishiwata, Y. Matsui, and Y. Tokura, Near room-temperature formation of a skyrmion crystal in thin-films of the helimagnet FeGe, Nat. Mater. **10**, 106 (2011).

[18] T. Adams, A. Chacon, M. Wagner, A. Bauer, G. Brandl, B. Pedersen, H. Berger, P. Lemmens, and C. Pfleiderer, Long-wavelength helimagnetic order and skyrmion lattice phase in Cu_2OSeO_3, Phys. Rev. Lett. **108**, 237204 (2012).

[19] S. Seki, X. Z. Yu, S. Ishiwata, and Y. Tokura, Observation of skyrmions in a multiferroic material, Science **336**, 198 (2012).

[20] X. Z. Yu, Y. Onose, N. Kanazawa, J. H. Park, J. H. Han, Y. Matsui, N. Nagaosa, and Y. Tokura, Real-space observation of a two-dimensional skyrmion crystal, Nature (London) **465**, 901 (2010).

[21] J. Bouaziz, E. Mendive-Tapia, S. Blügel, and J. B. Staunton, Fermi-surface origin of skyrmion lattices in centrosymmetric rare-earth intermetallics, Phys. Rev. Lett. **128**, 157206 (2022).

[22] N. D. Khanh, T. Nakajima, S. Hayami, S. Gao, Y. Yamasaki, H. Sagayama, H. Nakao, R. Takagi, Y. Motome, Y. Tokura, T.-H. Arima, and S. Seki, Zoology of multiple-Q spin textures in a centrosymmetric tetragonal magnet with itinerant electrons, Adv. Sci. **9**, 2105452 (2022).

[23] G. D. A. Wood, D. D. Khalyavin, D. A. Mayoh, J. Bouaziz, A. E. Hall, S. J. R. Holt, F. Orlandi, P. Manuel, S. Blügel, J. B. Staunton, O. A. Petrenko, M. R. Lees, and G. Balakrishnan, Double-Q ground state with topological charge stripes in the centrosymmetric skyrmion candidate $GdRu_2Si_2$, Phys. Rev. B **107**, L180402 (2023).

[24] J. Spethmann, N. D. Khanh, H. Yoshimochi, R. Takagi, S. Hayami, Y. Motome, R. Wiesendanger, S. Seki, and K. von Bergmann, SP-STM Study of the Multi-Q Phases in $GdRu_2Si_2$, Phys. Rev. Mater. **8**, 064404 (2024).

[25] S. Hayami and Y. Motome, Topological spin crystals by itinerant frustration, J. Phys.: Condens. Matter. **33**, 443001 (2021).

[26] M. S. Torikachvili, S. L. Bud'ko, N. Ni, and P. C. Canfield, Pressure induced superconductivity in $CaFe_2As_2$, Phys. Rev. Lett. **101**, 057006 (2008).

[27] Y. W. Windsor, S.-E. Lee, D. Zahn, V. Borisov, D. Thonig, K. Kliemt, A. Ernst, C. Schüßler-Langeheine, N. Pontius, U. Staub, C. Krellner, D. V. Vyalikh, O. Eriksson, and L. Rettig, Exchange scaling of ultrafast angular momentum transfer in 4f antiferromagnets, Nat. Mater. **21**, 514 (2022).

[28] R. Hoffmann and C. Zheng, Making and breaking bonds in the solid state: The $ThCr_2Si_2$ structure, J. Phys. Chem. **89**, 4175 (1985).

[29] K. Hiebl, C. Horvath, P. Rogl, and M. J. Sienko, Magnetic properties and structural chemistry of ternary silicides (RE, Th, U) Ru_2Si_2 (RE = RARE EARTH), J. Magn. Magn. Mater. **37**, 287 (1983).

[30] P. E. Blöchl, Projector augmented-wave method, Phys. Rev. B **50**, 17953 (1994).

[31] G. Kresse and D. Joubert, From ultrasoft pseudopotentials to the projector augmented-wave method, Phys. Rev. B **59**, 1758 (1999).

[32] G. Kresse and J. Hafner, *Ab initio* molecular dynamics for liquid metals, Phys. Rev. B **47**, 558 (1993).

[33] G. Kresse and J. Hafner, *Ab initio* molecular-dynamics simulation of the liquid-metal–amorphous-semiconductor transition in germanium, Phys. Rev. B **49**, 14251 (1994).

[34] G. Kresse and J. Furthmüller, Efficient iterative schemes for *ab initio* total-energy calculations using a plane-wave basis set, Phys. Rev. B **54**, 11169 (1996).

[35] G. Kresse and J. Furthmüller, Efficiency of *ab-initio* total energy calculations for metals and semiconductors using a plane-wave basis set, Comput. Mater. Sci. **6**, 15 (1996).

[36] J. P. Perdew, K. Burke, and M. Ernzerhof, Generalized gradient approximation made simple, Phys. Rev. Lett. **77**, 3865 (1996).

[37] J. P. Perdew, K. Burke, and M. Ernzerhof, Generalized gradient approximation made simple, Phys. Rev. Lett. **78**, 1396(E) (1997).

[38] A. N. Anisimov, W. Platow, P. Poulopoulos, W. Wisny, M. Farle, K. Baberschke, P. Isberg, B. Hjörvarsson, and R. Wäppling, The temperature-dependent in- and out-of-plane magnetic anisotropies in superlattices, J. Phys.: Condens. Matter. **9**, 10581 (1997).

[39] G. Kotliar, S. Y. Savrasov, K. Haule, V. S. Oudovenko, O. Parcollet, and C. A. Marianetti, Electronic structure calculations with dynamical mean-field theory, Rev. Mod. Phys. **78**, 865 (2006).

[40] A. I. Liechtenstein, V. I. Anisimov, and J. Zaanen, Density-functional theory and strong interactions: Orbital ordering in Mott-Hubbard insulators, Phys. Rev. B **52**, R5467 (1995).

[41] T. Nomoto and R. Arita, *Ab initio* exploration of short-pitch skyrmion materials: Role of orbital frustration, J. Appl. Phys. **133**, 150901 (2023).

[42] J. M. Wills and B. R. Cooper, Synthesis of band and model Hamiltonian theory for hybridizing cerium systems, Phys. Rev. B **36**, 3809 (1987).

[43] J. M. Wills, O. Eriksson, M. Alouani, and D. L. Price, *Full-Potential LMTO Total Energy and Force Calculations in Electronic Structure and Physical Properties of Solids*, edited by H. Dreyssé (Springer-Verlag, Berlin Heidelberg, 2000), p. 148.

[44] J. M Wills, O. Eriksson, P. Andersson, A. Delin, O. Grechnyev, and M. Alouani, *Full-Potential Electronic Structure Method: Energy and Force Calculations with Density Functional and Dynamical Mean Field Theory* (Springer, Berlin, Heidelberg, 2010), Vol. 167.

[45] https://www.physics.uu.se/research/materials-theory/ongoing-research/code-development/rspt-main/.

[46] See Supplemental Material at http://link.aps.org/supplemental/10.1103/q853-plvr for a comparison of VASP and RSPT electronic structure calculations, a comparison of exchange interactions with and without spin-orbit coupling, the methodology for spin structure factor calculation, and additional data and figures on spin configurations and structure factors for different values of uniaxial anisotropy, which also contains Ref. [66].

[47] I. L. M. Locht, Y. O. Kvashnin, D. C. M. Rodrigues, M. Pereiro, A. Bergman, L. Bergqvist, A. I. Lichtenstein, M. I. Katsnelson, A. Delin, A. B. Klautau, B. Johansson, I. Di Marco, and O. Eriksson, Standard model of the rare earths analyzed from the Hubbard I approximation, Phys. Rev. B **94**, 085137 (2016).

[48] A. I. Liechtenstein, M. I. Katsnelson, V. P. Antropov, and V. A. Gubanov, Local spin density functional approach to the theory of exchange interactions in ferromagnetic metals and alloys, J. Magn. Magn. Mater. **67**, 65 (1987).

[49] Y. O. Kvashnin, O. Grånäs, I. Di Marco, M. I. Katsnelson, A. I. Lichtenstein, and O. Eriksson, Exchange parameters of strongly correlated materials: Extraction from spin-polarized density functional theory plus dynamical mean-field theory, Phys. Rev. B **91**, 125133 (2015).

[50] A. I. Lichtenstein and M. I. Katsnelson, Antiferromagnetism and *d*-wave superconductivity in cuprates: A cluster dynamical mean-field theory, Phys. Rev. B **62**, R9283 (2000).

[51] A. Szilva, Y. Kvashnin, E. A. Stepanov, L. Nordström, O. Eriksson, A. I. Lichtenstein, and M. I. Katsnelson, Quantitative theory of magnetic interactions in solids, Rev. Mod. Phys. **95**, 035004 (2023).

[52] G. H. O. Daalderop, P. J. Kelly, and M. F. H. Schuurmans, First-principles calculation of the magnetocrystalline anisotropy energy of iron, cobalt, and nickel, Phys. Rev. B **41**, 11919 (1990).

[53] V. Borisov, Y. O. Kvashnin, N. Ntallis, D. Thonig, P. Thunström, M. Pereiro, A. Bergman, E. Sjöqvist, A. Delin, L. Nordström, and O. Eriksson, Heisenberg and anisotropic exchange interactions in magnetic materials with correlated electronic structure and significant spin-orbit coupling, Phys. Rev. B **103**, 174422 (2021).

[54] B. Skubic, J. Hellsvik, L. Nordström, and O. Eriksson, A method for atomistic spin dynamics simulations: implementation and examples, J. Phys.: Condens. Matter. **20**, 315203 (2008).

[55] O. Eriksson, A. Bergman, L. Bergqvist, and J. Hellsvik, *Atomistic Spin Dynamics: Foundations and Applications* (Oxford University Press, Oxford, UK, 2017).

[56] J. Hellsvik, D. Thonig, K. Modin, D. Iuşan, A. Bergman, O. Eriksson, L. Bergqvist, and A. Delin, General method for atomistic spin-lattice dynamics with first-principles accuracy, Phys. Rev. B **99**, 104302 (2019).

[57] L. Landau and E. Lifshitz, 3 - on the theory of the dispersion of magnetic permeability in ferromagnetic bodies reprinted from physikalische zeitschrift der sowjetunion 8, part 2, 153, 1935. in *Perspectives in Theoretical Physics*, edited by L. P. Pitaevski (Pergamon, Amsterdam, 1992), p. 51.

[58] T. L. Gilbert, A phenomenological theory of damping in ferromagnetic materials, IEEE Trans. Magn. **40**, 3443 (2004).

[59] N. Hayashi, K. Saito, and Y. Nakatani, Calculation of demagnetizing field distribution based on fast fourier transform of convolution, Jpn. J. Appl. Phys. **35**, 6065 (1996).

[60] J. Jensen and A. R Mackintosh, *Rare Earth Magnetism: Structures and Excitations* (Oxford University Press, Oxford, 1991).

[61] Y. O. Kvashnin, R. Cardias, A. Szilva, I. Di Marco, M. I. Katsnelson, A. I. Lichtenstein, L. Nordström, A. B. Klautau, and O. Eriksson, Microscopic origin of Heisenberg and non-heisenberg exchange interactions in ferromagnetic bcc Fe, Phys. Rev. Lett. **116**, 217202 (2016).

[62] S. Sarkar, F. Cossu, P. Kumari, A. G. Moghaddam, A. Akbari, Y. O. Kvashnin, and I. Di Marco, Magnetism between magnetic adatoms on monolayer $NbSe_2$, 2D Mater. **9**, 045012 (2022).

[63] S. Sarkar, S. Sharma, O. Eriksson, and I. Di Marco, Understanding the nature of the magnetic coupling in transition metal doped Bi_2Se_3, Phys. Rev. B **110**, 064412 (2024).

[64] Y. Yasui, C. J. Butler, N. D. Khanh, S. Hayami, T. Nomoto, T. Hanaguri, Y. Motome, R. Arita, T.k. Arima, Y. Tokura *et al.*, Imaging the coupling between itinerant electrons and localised moments in the centrosymmetric skyrmion magnet $GdRu_2Si_2$, Nat. Commun. **11**, 5925 (2020).

[65] D. N. Aristov, Indirect RKKY interaction in any dimensionality, Phys. Rev. B **55**, 8064 (1997).

[66] S. Hayami and Y. Motome, Square skyrmion crystal in centrosymmetric itinerant magnets, Phys. Rev. B **103**, 024439 (2021).

[67] Y. S. Lin, P. J. Grundy, and E. A. Giess, Bubble domains in magnetostatically coupled garnet films, Appl. Phys. Lett. **23**, 485 (1973).

[68] T. Garel and S. Doniach, Phase transitions with spontaneous modulation-the dipolar Ising ferromagnet, Phys. Rev. B **26**, 325 (1982).

[69] S. Takao, A study of magnetization distribution of submicron bubbles in sputtered Ho-Co thin films, J. Magn. Magn. Mater. **31-34**, 1009 (1983).

[70] A. Garnier, D. Gignoux, N. Iwata, D. Schmitt, T. Shigeoka, and F. Y. Zhang, Anisotropic metamagnetism in $GdRu_2Si_2$, J. Magn. Magn. Mater. **140-144**, 899 (1995).

[71] K. Momma and F. Izumi, VESTA 3 for three-dimensional visualization of crystal, volumetric and morphology data, J. Appl. Crystallogr. **44**, 1272 (2011).

[72] Q. Xu, O. Eriksson, and A. Delin, SpinView: General interactive visual analysis tool for multiscale computational magnetism, arXiv:2309.17367.